First-principles calculations of the structural and electronic properties of monolayer $1T$-MoO$_2$ and WO$_2$

Yi-Chi Li [1] and Jian Zhou [1,2,*]

[1]*National Laboratory of Solid State Microstructures and Department of Materials Science and Engineering,*
Nanjing University, Nanjing 210093, China
[2]*Collaborative Innovation Center of Advanced Microstructures, Nanjing University, Nanjing 210093, China*

Two-dimensional transition metal dichalcogenides (TMDCs), such as MoS$_2$ and WTe$_2$, received extensive attention owing to their diverse crystal structures and intriguing physical properties. In contrast, there has been relatively limited research on transition-metal dioxides (TMDOs) despite sharing the same crystal structures with TMDCs. Here, we investigate the structural and electronic properties of monolayer T-phase MoO$_2$ and WO$_2$ using first-principles calculations. Our analysis reveals that their phonon dispersions have prominent imaginary modes, leading to the emergence of two charge density wave phases: $1T'$ and $\sqrt{3}\times\sqrt{3}$. Interestingly, we find that $1T'$-MoO$_2$ and WO$_2$ exhibit Dirac semimetal behavior, while their $\sqrt{3}\times\sqrt{3}$ phases are ferroelectric semiconductors, with out-of-plane spontaneous polarization of 3.99 and 3.94 pC/m, respectively. This work sheds light on structural and electronic properties of T-phase MoO$_2$ and WO$_2$, offering valuable insights for further experimental investigations into similar TMDOs materials.

I. INTRODUCTION

As an important member of two-dimensional (2D) materials, transition metal dichalcogenides (TMDCs) have been extensively studied due to their unique and diverse properties and applications [1–5]. Bulk TMDCs have a common chemical formula MX$_2$, where M represents transition metals and X is sulfur, selenium, or tellurium anions. TMDCs are van der Waals layered materials. Each layer features a sandwich structure with transition metals in the middle and chalcogen anions on both sides. Moreover, TMDCs exhibit different structures, corresponding to distinct physical properties [6–8]. For instance, the 2H phase MoS$_2$ is commonly observed in experiments [6,9], showing semiconducting behavior [10]. On the other hand, the metastable 1T phase MoS$_2$ has higher energy compared with the thermodynamically stable 2H phase. Despite this, it can still be synthesized in experiments and demonstrates superior conducting properties [11–13]. Additionally, TMDCs can also possess a T' phase, which can be considered as a charge density wave (CDW) structure from the original T phase. For example, monolayer WTe$_2$ adopts the T' structure at room temperature, exhibiting topological quantum spin Hall insulating properties [14,15]. Moreover, stacking two centrosymmetric T'-WTe$_2$ monolayers together will break the inversion symmetry, resulting in the emergence of unique ferroelectricity, known as sliding ferroelectricity [16,17].

While the T-phase MoS$_2$ can be synthesized in experiments, its phonon dispersion shows two prominent imaginary modes at the M($\frac{1}{2}$, 0, 0) and K ($\frac{1}{3}$, $\frac{1}{3}$, 0) points [18], leading to the formation of two low-energy CDW structures: the T' phase (2×1) and the d1T phase ($\sqrt{3}\times\sqrt{3}$), respectively [19,20]. Both structures have been successfully synthesized experimentally [21–23]. It is worth mentioning that the d1T phase TMDCs exhibit spontaneous polarization due to its noncentrosymmetric structure [18], which has been observed in experiment [8].

Compared to the extensively studied TMDCs, fewer studies have been conducted on 2D transition metal dioxides (TMDOs), possibly because they are usually metastable and difficult to synthesize by conventional experimental methods. In recent years, a number of 2D TMDOs have been reported experimentally and theoretically, including CoO$_2$ [24,25], FeO$_2$ [26], TiO$_2$ [27,28], RhO$_2$ [29,30], RuO$_2$ [31–33], NbO$_2$ [34], and IrO$_2$ [35,36]. In addition, theoretical studies have been systematically conducted on 2H-MoO$_2$ and WO$_2$ [37,38]. Given the potential for diverse structures and intriguing physical properties of 2D TMDOs, in this work, we focus on a systematic first-principles study of monolayer $1T$-MoO$_2$ and WO$_2$, as well as their CDW phases. Our calculations reveal that both materials exhibit two lower-energy CDW phases, namely T' and $\sqrt{3}\times\sqrt{3}$ phases, with the former being Dirac semimetals and the latter being ferroelectric semiconductors.

The organization of this paper is as follows: In Sec. II, we provide the details of the calculation methodology used in this work. In Sec. III, we discuss the crystal structures and CDW phases of $1T$-MoO$_2$ and WO$_2$. In the same section, we also explore the electronic and ferroelectric properties of the two CDW phases. Finally, we present a conclusion of this work in Sec. IV.

II. COMPUTATIONAL DETAILS

The structural and electronic properties of monolayer MoO$_2$ and WO$_2$ are carried out by the density functional

---
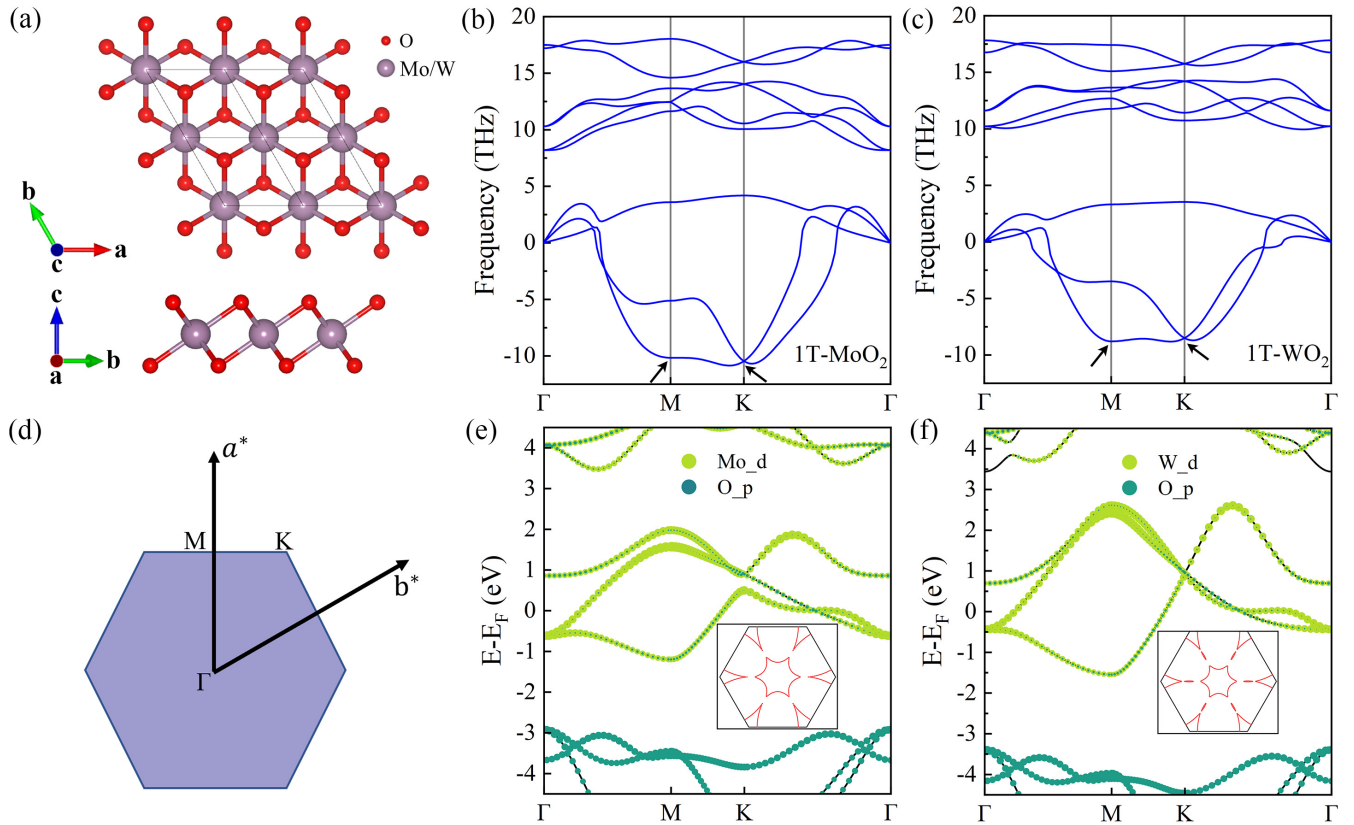
*Contact author: zhoujian@nju.edu.cn

FIG. 1. (a) Top and side views of crystal structures of monolayer $1T$-MoO_2 and WO_2, which are plotted by the VESTA code [58]. Phonon dispersions of monolayer (b) $1T$-MoO_2 and (c) $1T$-WO_2 at $T = 0$ K, where the arrows indicate two prominent imaginary phonon modes Q_M and Q_K at M and K points. (d) The Brillouin zone and the high-symmetry k points of $1T$-MoO_2 and WO_2. (e), (f) Calculated electronic band structures and Fermi surfaces of monolayer $1T$-MoO_2 and WO_2, respectively. The Fermi energy is set to zero.

theory (DFT) implemented in the Vienna *ab initio* simulation package (VASP) with the projector augmented wave method [39–42]. The calculations are performed within the generalized gradient approximation (GGA) with the Perdew-Burke-Ernzerhof (PBE) exchange-correlation functional [43]. The plane-wave cutoff energy is 520 eV. The Brillouin zone is sampled with a Γ-centered k mesh of $21\times21\times1$ for the $1T$ phase, $9\times16\times1$ for the $1T'$ phase, and $10\times10\times1$ for the $\sqrt{3}\times\sqrt{3}$ phase. The Fermi surfaces of the $1T$ phase MoO_2 and WO_2 are calculated with a fine k mesh of $101\times101\times1$. The crystal structures are fully relaxed until the force on each atom is less than 0.001 eV/Å and the electronic self-consistent convergence criteria is 10^{-7} eV. A vacuum space of 18 Å avoids the interaction between adjacent monolayers. Heyd-Scuseria-Ernzerhof (HSE06) hybrid functional [44,45] is also employed to obtain accurate bandgaps based on the optimized crystal structures from GGA-PBE calculations.

To examine the topological properties of the $1T'$-MoO_2 and WO_2, we have calculated the Berry curvatures of their Dirac points using the Fukui-Hatsugai-Suzuki method [46,47] implemented in the OPENMX code [48,49]. In the calculations, we use the crystal structures optimized by the VASP code, and the spin-orbit coupling (SOC) is considered.

Phonon dispersions are calculated by using the finite displacement method implemented in the PHONOPY code [50] to check the structural stability. A $6\times6\times1$ supercell is used in the phonon calculations at 0 K for the $1T$ phase while a

$3\times3\times1$ supercell is used for other phases. Furthermore, we also use the TDEP code [51]; it is based on *ab initio* molecular dynamics (AIMD) followed by mapping onto a model Hamiltonian that describes the lattice dynamics, to calculate the high-temperature phonon dispersions to estimate the temperature of the CDW phase transition. The AIMD calculations with canonical NVT ensemble are also performed to verify the thermal stability. The AIMD calculation lasts for 20 ps with a time step of 1.0 fs, and the temperature is set to 500 K, which is controlled by the Nosé-Hoover method [52]. The size of the simulated system is $6\times6\times1$, total of 108 atoms. The climbing image nudged elastic band (CI-NEB) method [53] is used to calculate the ferroelectric switching energy barrier. The method optimizes intermediate images along the reaction path by finding the lowest energy while maintaining equal spacing to neighboring images. The Berry phase method [54,55], by constructing intermediate phases, is employed to evaluate the ferroelectric polarization of the $\sqrt{3}\times\sqrt{3}$ phase.

III. RESULTS AND DISCUSSIONS

A. Crystal structures and electronic properties of $1T$-MoO_2 and WO_2

As shown in Fig. 1(a), the unit cell of $1T$-MoO_2 and WO_2 consists of three atoms, among which the Mo/W ions occupy the center of MO_6 octahedrons and are arranged in a triangular lattice. The optimized in-plane lattice constants of $1T$-MoO_2
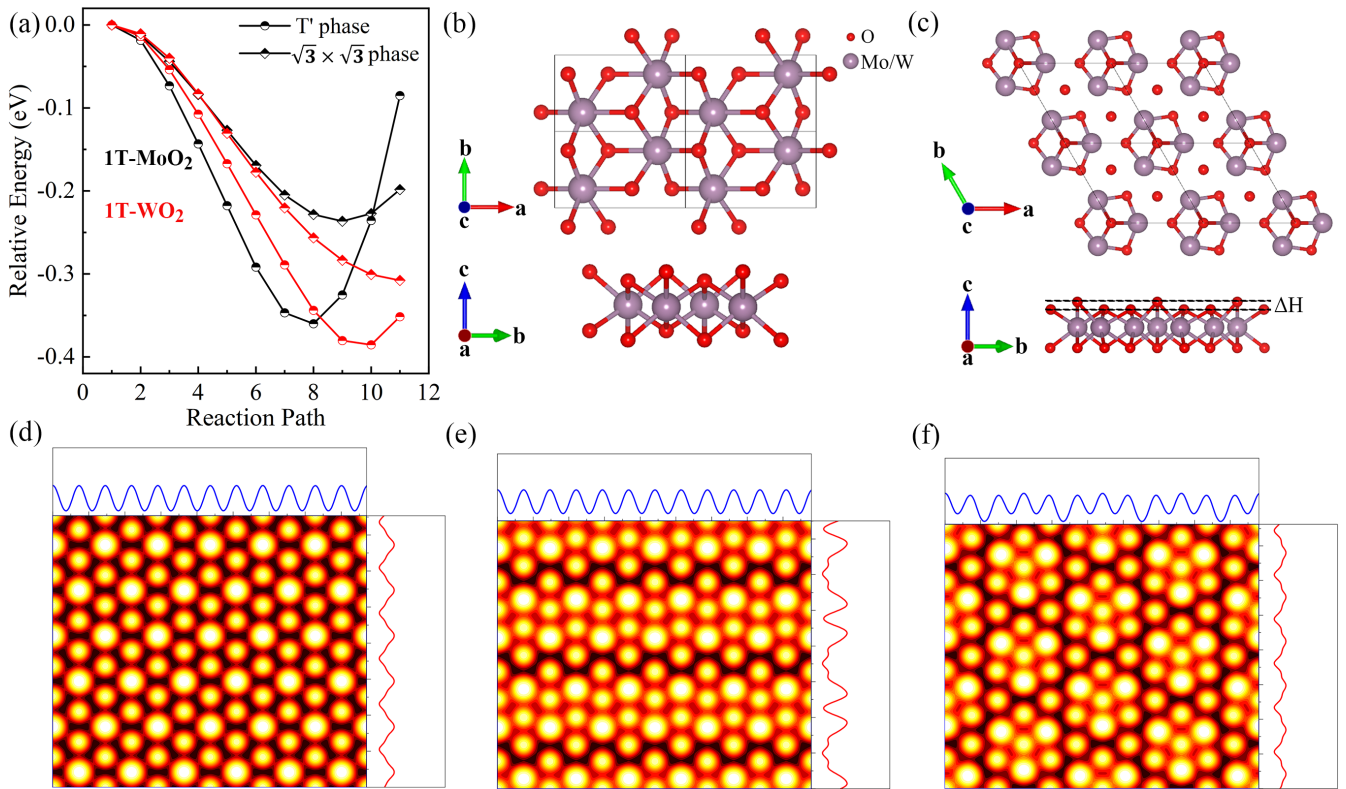
FIG. 2. (a) Calculated relative energies as a function of ions' displacements along the eigenvectors of the imaginary phonon modes of monolayer $1T$-MoO$_2$ and WO$_2$. (b), (c) Crystal structures of monolayer $1T'$ phase and $\sqrt{3}\times\sqrt{3}$ phase MoO$_2$ and WO$_2$. The ΔH in (c) represents the height difference of oxygen ions on the one side of the $\sqrt{3}\times\sqrt{3}$ phase MoO$_2$ and WO$_2$. (d)–(f) Charge density distributions of the $1T$, $1T'$, and $\sqrt{3}\times\sqrt{3}$ phases MoO$_2$.

are $a = b = 2.912$ Å and the length of the Mo–O bond is 2.049 Å. For the monolayer $1T$-WO$_2$, the optimized lattice constants are $a = b = 2.910$ Å and the length of the W–O bond is 2.065 Å. The lattice constants of $1T$-MoO$_2$ and WO$_2$ are $0.3 \sim 0.4$ Å smaller than those of $1T$-MX$_2$ (M=Mo, W; X=S, Se) [56,57], which is due to the stronger electronegativity and smaller anionic radius of the oxygen compared with those of sulfur and selenium anions.

Figures 1(b) and 1(c) present the phonon dispersions of $1T$-MoO$_2$ and WO$_2$, in which notable imaginary modes are observed at M and K points, labeled as Q$_M$ and Q$_K$, respectively. This implies that the $1T$-MoO$_2$ and WO$_2$ are unstable and possible CDW phase transitions are expected at low temperatures. Moreover, through AIMD simulations, we find that the total energies of $1T$-MoO$_2$ and WO$_2$ exhibit slight fluctuations at 500 K over a 20 ps period, as shown in Figs. S1(a) and (b) in the Supplemental Material [59]. This suggests that the $1T$-MoO$_2$ and WO$_2$ could be stable at elevated temperatures. We further analyzed the distribution of imaginary phonon modes in the Brillouin zone for $1T$-MoO$_2$ and WO$_2$ as shown in Fig. S2 in the Supplemental Material [59]. The results demonstrate that the chosen highly symmetric path Γ-M-K-Γ is representative, which can well reflect the minimum positions of the imaginary phonon modes.

Before discussing the CDW phase transitions of $1T$-MoO$_2$ and WO$_2$, we have calculated their electronic fatbands as shown in Figs. 1(e) and 1(f). Two electronic bands intersect the Fermi level, primarily attributed to the d orbitals of Mo

and W ions, confirming the metallic nature of $1T$-MoO$_2$ and WO$_2$. The Fermi surfaces of the two materials are depicted in the insets of Figs. 1(e) and 1(f), featuring triangular pockets near the K points and a hexagonal star around the Γ point.

B. CDW phase transitions of $1T$-MoO$_2$ and WO$_2$

Based on the vibrational eigenvectors of imaginary phonon modes Q$_M$ and Q$_K$, we can move the ions of $1T$-MoO$_2$ and WO$_2$ and calculate their total energies, as illustrated in Fig. 2(a). As the ions move, the energies decrease, suggesting the existence of structures with lower energies than the $1T$ phase. According to the relationship between the real and reciprocal lattice vectors, as depicted in Table S1 in the Supplemental Material [59], the imaginary phonon modes at the M and K points indicate CDW phases with 2×1 and $\sqrt{3}\times\sqrt{3}$ supercells, respectively.

Hence, we derive two CDW structures for monolayers MoO$_2$ and WO$_2$, namely, T' phase with space group P2$_1$/m (No. 11) and $\sqrt{3}\times\sqrt{3}$ phase with space group P31m (No. 157), as shown in Figs. 2(b) and 2(c), respectively. Table I presents the relative energies and lattice constants of different structures, with the energy of the ground structure being 0 eV. For the monolayer MoO$_2$, the ground structure is the $\sqrt{3}\times\sqrt{3}$ phase, with an energy of 0.495 eV lower than that of the undistorted $1T$ phase and 0.026 eV lower than that of the $1T'$ phase. Conversely, for the monolayer WO$_2$, the ground structure is the $1T'$ phase, with an energy of 0.547 eV lower

TABLE I. Calculated relative energies per formula unit, lattice constants of $1T$, $1T'$, and $\sqrt{3}\times\sqrt{3}$ phases of monolayer MoO_2 and WO_2.

Materials	Energy (eV)	Lattice constant (Å)
$1T$-MoO_2	0.495	$a = b = 2.912$
$1T'$-MoO_2	0.026	$a = 5.025$, $b = 2.942$
$\sqrt{3}\times\sqrt{3}$-MoO_2	0	$a = b = 5.102$
$1T$-WO_2	0.547	$a = b = 2.910$
$1T'$-WO_2	0	$a = 5.061$, $b = 2.954$
$\sqrt{3}\times\sqrt{3}$-WO_2	0.018	$a = b = 5.126$

than that of the undistorted $1T$ phase and 0.018 eV lower than that of the $\sqrt{3}\times\sqrt{3}$ phase. The above results are similar to those of MoS_2 and WS_2. Singh *et al.* discovered that in MoS_2, the energy of the $\sqrt{3}\times\sqrt{3}$ phase is lower than that of $1T'$ phase, whereas the opposite holds true for WS_2 [20]. We have also calculated the Helmholtz free energy (Table S2 in the Supplemental Material [59]) at 0 and 300 K for different phases and find that the ground state of the MoO_2 and WO_2 is not changed at 300 K.

Figures 2(d)–2(f) illustrate the periodic modulation of charge density in real space for the three structures, providing intuitive insight into the CDW superstructures. It is observed that the charge density of the $1T'$ phase is modulated along one direction only, while in the $\sqrt{3}\times\sqrt{3}$ phase, it shows obvious modulation in both directions.

Moreover, we have verified that the two CDW structures of MoO_2 and WO_2 are stable since their phonon dispersions have no imaginary modes, as shown in Figs. 3(a) and 3(b) and Fig. S3 in the Supplemental Material [59], respectively. Additionally, we have estimated the CDW transition temperature by analyzing the phonon dispersion at finite temperatures. For instance, in Fig. 3(c), the phonon dispersion of undistorted $1T$-MoO_2 at 300 K has imaginary modes, while it does not at 350 K. This suggests that the CDW transition temperature of $1T$-MoO_2 is between 300 and 350 K. Similarly, the CDW transition temperature of $1T$-WO_2 falls between 350 and 400 K, as depicted in Fig. S3(c) in the Supplemental Material [59].

Subsequently, we would like to discuss the underlying mechanism behind the CDW transition of $1T$-MoO_2 and WO_2. Conventionally, the Fermi surface nesting (FSN) is regarded as one of the origins of the CDW in materials [60,61]. The FSN can be quantified by the nesting factor ($\mathrm{Im}\chi_q$) and bare static susceptibility ($\mathrm{Re}\chi_q$), as defined [34]:

$$\mathrm{Im}\chi_q = \sum_k \delta(\varepsilon_k - E_F)\delta(\varepsilon_{k+q} - E_F), \qquad (1)$$

$$\mathrm{Re}\chi_q = \sum_k \frac{f(\varepsilon_k) - f(\varepsilon_{k+q})}{\varepsilon_k - \varepsilon_{k+q}}, \qquad (2)$$

in which the real (imaginary) part of electron susceptibility χ_q is $\mathrm{Re}\chi_q$ ($\mathrm{Im}\chi_q$) and $\delta(x)$ is numerically approximated by

$$\delta(x) \approx \frac{1}{\pi}\frac{\epsilon}{\epsilon^2 + x^2}, \qquad (3)$$

where ε_k is the eigenvalue of the Kohn-Sham equation, E_F is the Fermi level, and f stands for the Fermi-Dirac distribution function. In our calculations, we set ϵ to a constant value of 0.02.

Figures 4(a) and 4(b) illustrate the distribution of the negative $\mathrm{Re}\chi_q$ and $\mathrm{Im}\chi_q$ in the Brillouin zone for $1T$-MoO_2. To provide a more quantitative analysis of electron susceptibility χ_q, we extracted the corresponding data along the high symmetry Γ-M-K-Γ path as depicted in Figs. 4(c) and 4(d). The electron susceptibility χ_q of $1T$-WO_2 can be found in Fig. S4 in the Supplemental Material [59]. Notably, prominent peaks in negative $\mathrm{Re}\chi_q$ and $\mathrm{Im}\chi_q$ are observed at the K point, consistent with the imaginary phonon mode Q_K. This suggests that the $\sqrt{3}\times\sqrt{3}$ CDW phase is primarily driven by the FSN. However, there are no peaks at the M point in the negative $\mathrm{Re}\chi_q$ and $\mathrm{Im}\chi_q$, which indicate that the FSN does not drive the $1T'$ CDW phase at Q_M.

C. Electronical properties of the $1T'$ phase MoO_2 and WO_2

In what follows, we would like to discuss the electronic properties of the $1T'$ phase and $\sqrt{3}\times\sqrt{3}$ CDW phase of monolayer MoO_2 and WO_2. The electronic band structures of $1T'$-MoO_2 and WO_2 are depicted in Figs. 5(a) and 5(b), respectively. Notably, two Dirac points can be observed along the Y-Γ and R-X paths in both materials. One Dirac point
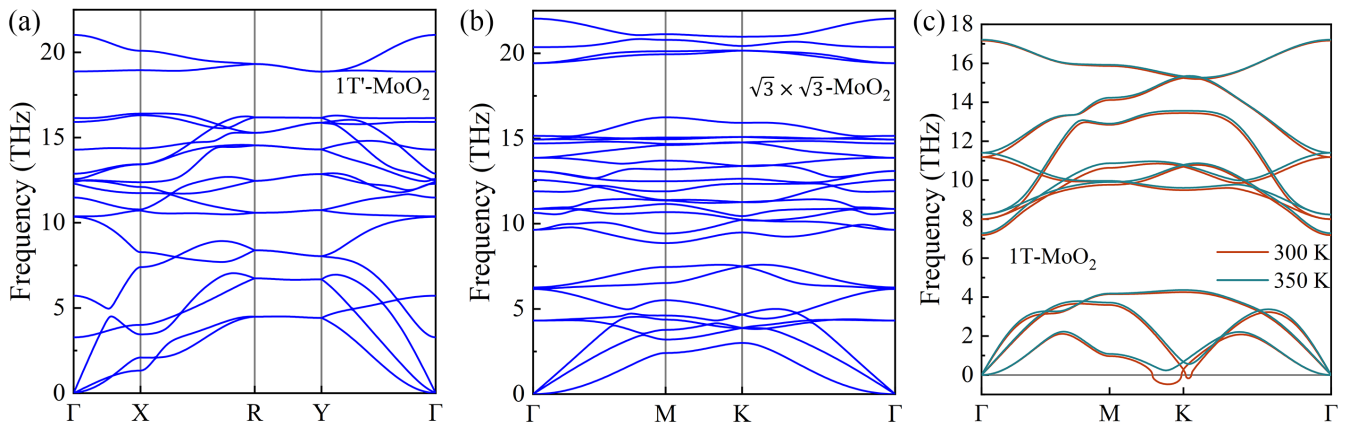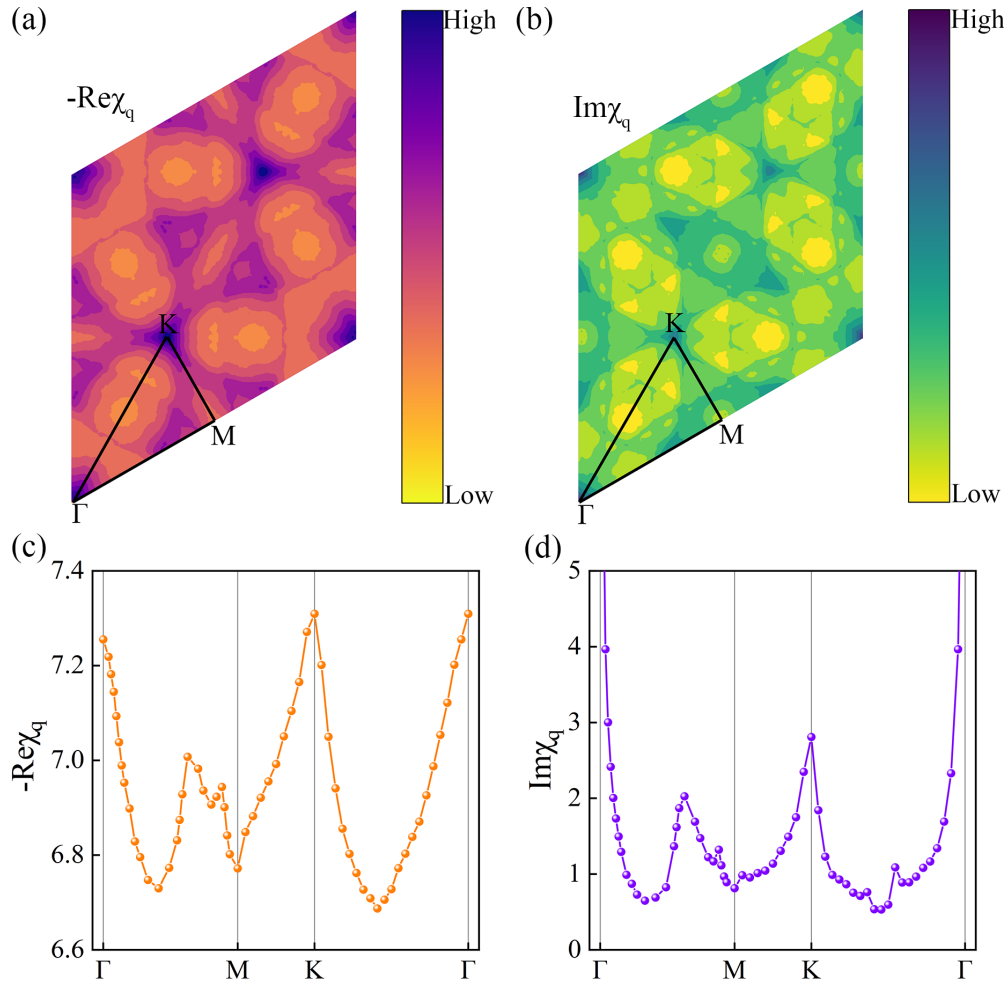

FIG. 3. (a), (b) Calculated phonon dispersions of $1T'$ and $\sqrt{3}\times\sqrt{3}$ phase MoO_2 at 0 K. (c) Calculated phonon dispersions of $1T$-MoO_2 at 300 and 350 K.

FIG. 4. (a), (b) Calculated negative $\mathrm{Re}\chi_q$ and $\mathrm{Im}\chi_q$ of $1T$-MoO$_2$ in the Brillouin zone. (c), (d) Calculated negative $\mathrm{Re}\chi_q$ and $\mathrm{Im}\chi_q$ of $1T$-MoO$_2$ along the Γ-M-K-Γ path.

resides approximately 0.3 eV above the Fermi energy, while the other is around 0.2 eV below the Fermi energy. Good linear band structures can be found around the Fermi energy. More detailed electronic band structures near the Dirac points are depicted in Figs. S5 and S6 in the Supplemental Material [59]. Upon considering the SOC effect, the degeneracy of the Dirac point is broken, and energy gaps of about 45 and 35 meV occur for the $1T'$-MoO$_2$ along the Y-Γ and R-X, respectively. Due to the larger SOC effect in W ions, the energy gaps of $1T'$-WO$_2$ are much larger, reaching about 145 and 120 meV along the respective directions. Additionally, we have also calculated the Berry curvatures of $1T'$-MoO$_2$ and WO$_2$, as shown in Figs. 5(c) and 5(d). Significant nonzero Berry curvatures can be found and confirm the nontrivial properties of the Dirac points.

Similar Dirac points are also present in $1T'$-MoS$_2$ and WTe$_2$, although they are very close to the Fermi energy. Upon considering the SOC effect, they become quantum spin Hall insulators [14]. In contrast, the SOC-induced energy gaps in $1T'$-MoO$_2$ and WO$_2$ shift upward and downward by approximately 0.3 and 0.2 eV, and they maintain semimetallic properties with linear dispersion around the Fermi energy.

This suggests that the influence of SOC on the electronic properties of the $1T'$-MoO$_2$ and WO$_2$ is relatively small.

D. Ferroelectricity of the $\sqrt{3}\times\sqrt{3}$ phase MoO$_2$ and WO$_2$

Unlike the $1T'$ phase, the $\sqrt{3}\times\sqrt{3}$ phase MoO$_2$ and WO$_2$ have markedly different electronic properties. Figure 6(a) presents the electronic band structure of the $\sqrt{3}\times\sqrt{3}$ phase MoO$_2$, revealing its semiconductor nature with a bandgap of approximately 1.0 eV in the standard PBE calculations. Notably, this bandgap is nearly twice as large as that of $\sqrt{3}\times\sqrt{3}$ phase MoS$_2$, which is reported to be 0.57 eV in the similar PBE calculations [62]. Considering that the PBE functional usually seriously underestimates bandgaps, we also utilize the HSE06 hybrid functional to calculate the electronic band structure of $\sqrt{3}\times\sqrt{3}$ phase MoO$_2$, where its bandgap increases significantly to about 2.4 eV. Similarly, the electronic band structures of $\sqrt{3}\times\sqrt{3}$ phase WO$_2$ are also calculated as shown in Fig. 6(b), where its bandgap is 1.2 and 2.3 eV from the PBE and HSE06 functionals.

Of particular significance, $\sqrt{3}\times\sqrt{3}$ phase MoO$_2$ and WO$_2$ possesses a noncentrosymmetric point group C$_{3v}$, suggesting
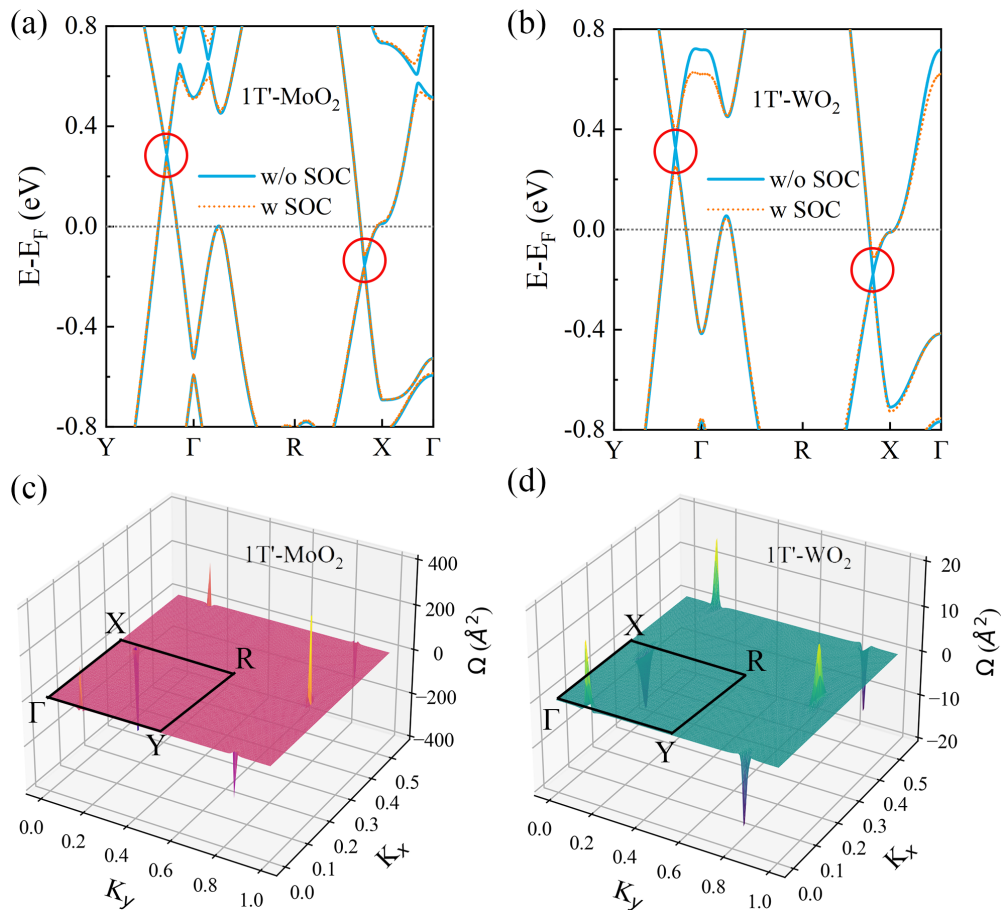
FIG. 5. Electronic band structure of (a) $1T'$-MoO$_2$ and (b) $1T'$-WO$_2$ with and without SOC effect. The red circles represent the locations of the Dirac points. Calculated Berry curvature of (c) $1T'$-MoO$_2$ and (d) $1T'$-WO$_2$.

that they could be ferroelectric. Its asymmetric structure along the out-of-plane direction can be clearly seen from its side view depicted in Fig. 2(c). Performing a horizontal mirror symmetry operation on this structure yields another structure with the same energy but opposite polarization. These two structures can be converted into each other through the undistorted $1T$ phase. As shown in Fig. S7 in the Supplemental Material [59], the NEB calculations between the two ferroelectric states indicate a moderate energy barrier of approximately 0.5 eV/f.u., slightly higher than those of MoS$_2$ and WSe$_2$,

which are 0.28 and 0.32 eV/f.u., respectively [20]. The Berry phase calculations reveal that spontaneous polarizations are 3.99 and 3.94 pC/m along the out-of-plane direction for the $\sqrt{3}\times\sqrt{3}$ phase of MoO$_2$ and WO$_2$, respectively. These values surpass those of $\sqrt{3}\times\sqrt{3}$ phase MX$_2$ (M = Mo/W; X=S, Se, Te) in the range of 0.8 to 1.1 pC/m [63] and bilayer WTe$_2$ (0.38 pC/m) [64,65]. We think the larger spontaneous polarizations in $\sqrt{3}\times\sqrt{3}$ phase MoO$_2$ and WO$_2$ could be due to the large structural distortion. It is found that the height differences of the anions along the out-of-plane direction [ΔH in Fig. 2(c)] in MoO$_2$ and WO$_2$ are much larger than those of MoS$_2$ and WSe$_2$. For example, the ΔH of MoO$_2$ is about 0.42 Å while the one of MoS$_2$ is only 0.27 Å from our calculations. The large structural distortion in MoO$_2$ and WO$_2$ could be attributed to the large electronegativity and small radius of the oxygen anion compared with those of sulfur and selenium anions.

IV. CONCLUSION

We have conducted a systematic investigation of the structural and electronic properties of monolayer $1T$ phase MoO$_2$ and WO$_2$ using first-principles calculations. Our analysis reveals that both materials display instability at low temperatures, resulting in periodic modulation of charge density and the emergence of two distinct CDW phases: $1T'$
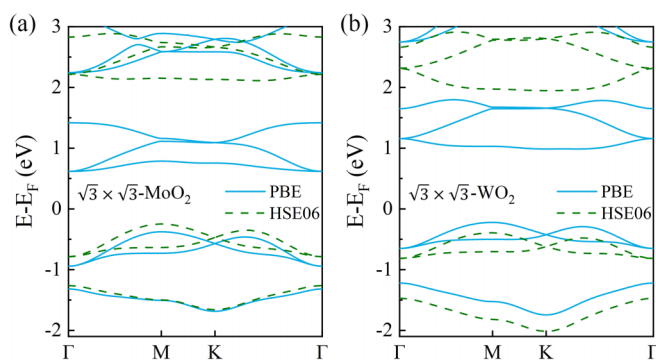

FIG. 6. (a) Electronic band structure of $\sqrt{3}\times\sqrt{3}$-MoO$_2$ and (b) $\sqrt{3}\times\sqrt{3}$-WO$_2$ by the PBE and HSE06 hybrid calculations.

and $\sqrt{3}\times\sqrt{3}$. Both CDW phases exhibit dynamic stability and much lower energies than the undistorted $1T$ phase. Our calculations indicate that $1T'$ phase MoO_2 and WO_2 are Dirac semimetals, while their $\sqrt{3}\times\sqrt{3}$ phases are ferroelectric semiconductors. The $\sqrt{3}\times\sqrt{3}$ phase MoO_2 and WO_2 demonstrate out-of-plane spontaneous polarizations of 3.99 and 3.94 pC/m, respectively, with corresponding bandgaps of 2.4 and 2.3 eV. This study extends the research of 2D transition metal dichalcogenides to the much less studied 2D transition metal dioxides. Our findings lay a foundation for further theoretical and experimental studies on similar materials.

[1] J. Wilson, F. Di Salvo, and S. Mahajan, Charge-density waves in metallic, layered, transition-metal dichalcogenides, Phys. Rev. Lett. **32**, 882 (1974).

[2] R. Coleman, B. Giambattista, P. Hansma, A. Johnson, W. McNairy, and C. Slough, Scanning tunnelling microscopy of charge-density waves in transition metal chalcogenides, Adv. Phys. **37**, 559 (1988).

[3] I. Guillamón, H. Suderow, S. Vieira, L. Cario, P. Diener, and P. Rodiere, Superconducting density of states and vortex cores of 2H-NbS$_2$, Phys. Rev. Lett. **101**, 166407 (2008).

[4] X.-L. Qi and S.-C. Zhang, Topological insulators and superconductors, Rev. Mod. Phys. **83**, 1057 (2011).

[5] B. Radisavljevic, A. Radenovic, J. Brivio, V. Giacometti, and A. Kis, Single-layer MoS$_2$ transistors, Nat. Nanotechnol. **6**, 147 (2011).

[6] R. Lv, J. A. Robinson, R. E. Schaak, D. Sun, Y. Sun, T. E. Mallouk, and M. Terrones, Transition metal dichalcogenides and beyond: Synthesis, properties, and applications of single- and few-layer nanosheets, Acc. Chem. Res. **48**, 56 (2015).

[7] M. N. Ali, J. Xiong, S. Flynn, J. Tao, Q. D. Gibson, L. M. Schoop, T. Liang, N. Haldolaarachchige, M. Hirschberger, N. P. Ong *et al.*, Large, non-saturating magnetoresistance in WTe$_2$, Nature (London) **514**, 205 (2014).

[8] S. Yuan, X. Luo, H. L. Chan, C. Xiao, Y. Dai, M. Xie, and J. Hao, Room-temperature ferroelectricity in MoTe$_2$ down to the atomic monolayer limit, Nat. Commun. **10**, 1775 (2019).

[9] X. Fan, P. Xu, D. Zhou, Y. Sun, Y. C. Li, M. A. T. Nguyen, M. Terrones, and T. E. Mallouk, Fast and efficient preparation of exfoliated 2H-MoS$_2$ nanosheets by sonication-assisted lithium intercalation and infrared laser-induced 1T to 2H phase reversion, Nano Lett. **15**, 5956 (2015).

[10] K. F. Mak, C. Lee, J. Hone, J. Shan, and T. F. Heinz, Atomically thin MoS$_2$: A new direct-gap semiconductor, Phys. Rev. Lett. **105**, 136805 (2010).

[11] J. Heising and M. G. Kanatzidis, Structure of restacked MoS$_2$ and WS$_2$ elucidated by electron crystallography, J. Am. Chem. Soc. **121**, 638 (1999).

[12] M. Acerce, D. Voiry, and M. Chhowalla, Metallic 1T phase MoS$_2$ nanosheets as supercapacitor electrode materials, Nat. Nanotechnol. **10**, 313 (2015).

[13] W. Ding, L. Hu, J. Dai, X. Tang, R. Wei, Z. Sheng, C. Liang, D. Shao, W. Song, Q. Liu *et al.*, Highly ambient-stable 1T-MoS$_2$ and 1T-WS$_2$ by hydrothermal synthesis under high magnetic fields, ACS Nano **13**, 1694 (2019).

[14] X. Qian, J. Liu, L. Fu, and J. Li, Quantum spin Hall effect in two-dimensional transition metal dichalcogenides, Science **346**, 1344 (2014).

[15] S. Tang, C. Zhang, D. Wong, Z. Pedramrazi, H.-Z. Tsai, C. Jia, B. Moritz, M. Claassen, H. Ryu, S. Kahn *et al.*, Quantum spin Hall state in monolayer 1T'-WTe$_2$, Nat. Phys. **13**, 683 (2017).

[16] Z. Fei, W. Zhao, T. A. Palomaki, B. Sun, M. K. Miller, Z. Zhao, J. Yan, X. Xu, and D. H. Cobden, Ferroelectric switching of a two-dimensional metal, Nature (London) **560**, 336 (2018).

[17] P. Sharma, F.-X. Xiang, D.-F. Shao, D. Zhang, E. Y. Tsymbal, A. R. Hamilton, and J. Seidel, A room-temperature ferroelectric semimetal, Sci. Adv. **5**, eaax5080 (2019).

[18] S. N. Shirodkar and U. V. Waghmare, Emergence of ferroelectricity at a metal-semiconductor transition in a 1T monolayer of MoS$_2$, Phys. Rev. Lett. **112**, 157601 (2014).

[19] C. Rovira and M. H. Whangbo, Factors governing the charge density wave patterns of layered transition-metal compounds of octahedral coordination with d2 and d3 electron counts, Inorg. Chem. **32**, 4094 (1993).

[20] A. Singh, S. N. Shirodkar, and U. V. Waghmare, 1H and 1T polymorphs, structural transitions and anomalous properties of (Mo, W)(S, Se)$_2$ monolayers: First-principles analysis, 2D Mater. **2**, 035013 (2015).

[21] F. Wypych, T. Weber, and R. Prins, Scanning tunneling microscopic investigation of 1T-MoS$_2$, Chem. Mater. **10**, 723 (1998).

[22] Y. Yu, G.-H. Nam, Q. He, X.-J. Wu, K. Zhang, Z. Yang, J. Chen, Q. Ma, M. Zhao, Z. Liu *et al.*, High phase-purity 1T'-MoS$_2$-and 1T'-MoSe$_2$-layered crystals, Nat. Chem. **10**, 638 (2018).

[23] L. Liu, J. Wu, L. Wu, M. Ye, X. Liu, Q. Wang, S. Hou, P. Lu, L. Sun, J. Zheng *et al.*, Phase-selective synthesis of 1T'-MoS$_2$ monolayers and heterophase bilayers, Nat. Mater. **17**, 1108 (2018).

[24] T. Motohashi, Y. Katsumata, T. Ono, R. Kanno, M. Karppinen, and H. Yamauchi, Synthesis and properties of CoO$_2$, the $x = 0$ end member of the Li$_x$CoO$_2$ and Na$_x$CoO$_2$ systems, Chem. Mater. **19**, 5063 (2007).

[25] L. Liang, S. Du, L. Wang, Z. Liu, J. Wu, and S. Zhang, Tunable magnetic and electronic properties of the 2D CoO$_2$ layer, J. Phys. Chem. C **125**, 873 (2021).

[26] B. Zhang, X. Chen, F. Deng, X. Lv, C. Zhang, B. Zheng, H. Wang, and J. Wang, Spin direction tunable topological transition in two-dimensional frustrate antiferromagnetic triangular lattice T-FeO$_2$ monolayer, Appl. Phys. Lett. **121**, 232405 (2022).

[27] B. Y. Zhang, K. Xu, Q. Yao, A. Jannat, G. Ren, M. R. Field, X. Wen, C. Zhou, A. Zavabeti, and J. Z. Ou, Hexagonal metal oxide monolayers derived from the metal–gas interface, Nat. Mater. **20**, 1073 (2021).

[28] X. Bu, H. Liu, and Y. Li, Stable phases of freestanding monolayer TiO_2: Emergence of out-of-plane ferroelectricity, Phys. Rev. B **109**, 165435 (2024).

[29] J. Shi, Q. Sun, W. Zhu, T. Cheng, F. Liao, M. Ma, J. Yang, H. Yang, Z. Fan, and M. Shao, Lattice stain dominated hydrazine oxidation reaction in single-metal-element nanosheet, Chem. Eng. J. **463**, 142385 (2023).

[30] H. Lee and M. Choi, Out-of-plane ferromagnetism in two-dimensional $1T$-RhO_2, Phys. Rev. B **106**, 064414 (2022).

[31] K. Sonobe, S. Tominaka, and W. Sugimoto, Symmetric breakage-induced semimetallic state: Polymorphism in ruthenate nanosheets, J. Am. Chem. Soc. **144**, 15008 (2022).

[32] Y. Wang, F. Li, H. Zheng, X. Han, and Y. Yan, Large magnetic anisotropy and its strain modulation in two-dimensional intrinsic ferromagnetic monolayer RuO_2 and OsO_2, Phys. Chem. Chem. Phys. **20**, 28162 (2018).

[33] G.-Z. Liu, S.-T. Sun, Y. B. Chen, S.-H. Yao, and J. Zhou, First-principles studies on the crystal structure and electronic properties of two-dimensional RuO_2 and OsO_2, Phys. Rev. B **109**, 075411 (2024).

[34] Y.-C. Li and J. Zhou, Predicted multiple charge density wave phases in monolayer $1T$-NbO_2, J. Phys.: Condens. Matter **36**, 185702 (2024).

[35] A. Smolyanyuk, M. Aichhorn, I. I. Mazin, and L. Boeri, *Ab initio* prediction of a two-dimensional variant of the iridate IrO_2, Phys. Rev. B **100**, 235114 (2019).

[36] Q. Dang, H. Lin, Z. Fan, L. Ma, Q. Shao, Y. Ji, F. Zheng, S. Geng, S.-Z. Yang, N. Kong *et al.*, Iridium metallene oxide for acidic oxygen evolution catalysis, Nat. Commun. **12**, 6007 (2021).

[37] W. Fang, X. Xiao, H. Wei, Y. Chen, M. Li, and Y. He, The elastic, electron, phonon, and vibrational properties of monolayer XO_2 (X= Cr, Mo, W) from first principles calculations, Mater. Today Commun. **30**, 103183 (2022).

[38] Á. H. Tobar, J. F. Murillo G, C. O. López, J. A. R. Martínez, and M. J. Espitia R, Study of the structural and electronic properties of three-and two-dimensional transition-metal dioxides using first-principles calculations, Comput. Condens. Matter **25**, e00498 (2020).

[39] G. Kresse and J. Furthmüller, Efficient iterative schemes for *ab initio* total-energy calculations using a plane-wave basis set, Phys. Rev. B **54**, 11169 (1996).

[40] G. Kresse and J. Furthmüller, Efficiency of ab-initio total energy calculations for metals and semiconductors using a plane-wave basis set, Comput. Mater. Sci. **6**, 15 (1996).

[41] P. E. Blöchl, Projector augmented-wave method, Phys. Rev. B **50**, 17953 (1994).

[42] G. Kresse and D. Joubert, From ultrasoft pseudopotentials to the projector augmented-wave method, Phys. Rev. B **59**, 1758 (1999).

[43] J. P. Perdew, K. Burke, and M. Ernzerhof, Generalized gradient approximation made simple, Phys. Rev. Lett. **77**, 3865 (1996).

[44] J. Heyd, G. E. Scuseria, and M. Ernzerhof, Hybrid functionals based on a screened Coulomb potential, J. Chem. Phys. **118**, 8207 (2003).

[45] A. V. Krukau, O. A. Vydrov, A. F. Izmaylov, and G. E. Scuseria, Influence of the exchange screening parameter on the performance of screened hybrid functionals, J. Chem. Phys. **125**, 224106 (2006).

[46] H. Sawahata, N. Yamaguchi, H. Kotaka, and F. Ishii, First-principles study of electric-field-induced topological phase transition in one-bilayer Bi(111), Jpn. J. Appl. Phys. **57**, 030309 (2018).

[47] T. Fukui, Y. Hatsugai, and H. Suzuki, Chern numbers in discretized Brillouin zone: Efficient method of computing (spin) Hall conductances, J. Phys. Soc. Jpn. **74**, 1674 (2005).

[48] T. Ozaki, Variationally optimized atomic orbitals for large-scale electronic structures, Phys. Rev. B **67**, 155108 (2003).

[49] T. Ozaki and H. Kino, Numerical atomic basis orbitals from H to Kr, Phys. Rev. B **69**, 195113 (2004).

[50] A. Togo and I. Tanaka, First principles phonon calculations in materials science, Scr. Mater. **108**, 1 (2015).

[51] O. Hellman, I. A. Abrikosov, and S. I. Simak, Lattice dynamics of anharmonic solids from first principles, Phys. Rev. B **84**, 180301(R) (2011).

[52] G. J. Martyna, M. L. Klein, and M. Tuckerman, Nosé–Hoover chains: The canonical ensemble via continuous dynamics, J. Chem. Phys. **97**, 2635 (1992).

[53] G. Henkelman, B. P. Uberuaga, and H. Jónsson, A climbing image nudged elastic band method for finding saddle points and minimum energy paths, J. Chem. Phys. **113**, 9901 (2000).

[54] R. D. King-Smith and D. Vanderbilt, Theory of polarization of crystalline solids, Phys. Rev. B **47**, 1651 (1993).

[55] R. Resta, Macroscopic polarization in crystalline dielectrics: The geometric phase approach, Rev. Mod. Phys. **66**, 899 (1994).

[56] W. Zhao and F. Ding, Energetics and kinetics of phase transition between a 2H and a 1T MoS_2 monolayer—A theoretical study, Nanoscale **9**, 2301 (2017).

[57] F. Güller, A. M. Llois, J. Goniakowski, and C. Noguera, Prediction of structural and metal-to-semiconductor phase transitions in nanoscale MoS_2, WS_2, and other transition metal dichalcogenide zigzag ribbons, Phys. Rev. B **91**, 075407 (2015).

[58] K. Momma and F. Izumi, *Vesta 3* for three-dimensional visualization of crystal, volumetric and morphology data, J. Appl. Cryst. **44**, 1272 (2011).

[59] See Supplemental Material at http://link.aps.org/supplemental/10.1103/PhysRevB.110.045447 for details of the AIMD simulations of $1T-MoO_2$ and WO_2, distribution of phonon imaginary modes in the Brillouin zone of $1T-MoO_2$ and WO_2, electron susceptibility of the $1T-WO_2$, electronic band structures near the Dirac points of the $1T'-MoO_2$ and WO_2.

[60] X. Zhu, Y. Cao, J. Zhang, E. Plummer, and J. Guo, Classification of charge density waves based on their nature, Proc. Natl. Acad. Sci. USA **112**, 2367 (2015).

[61] M. D. Johannes and I. I. Mazin, Fermi surface nesting and the origin of charge density waves in metals, Phys. Rev. B **77**, 165135 (2008).

[62] H. L. Zhuang, M. D. Johannes, A. K. Singh, and R. G. Hennig, Doping-controlled phase transitions in single-layer MoS_2, Phys. Rev. B **96**, 165305 (2017).

[63] W. Zhou, A. Li, S. Peng, and F. Ouyang, First-principle studies on the ferroelectricity and gate-controlled Rashba spin-orbit coupling of d1T-phase transition-metal dichalcogenide monolayers, Physica E **134**, 114934 (2021).

[64] Q. Yang, M. Wu, and J. Li, Origin of two-dimensional vertical ferroelectricity in WTe_2 bilayer and multilayer, J. Phys. Chem. Lett. **9**, 7160 (2018).

[65] H. Wang and X. Qian, Ferroelectric nonlinear anomalous Hall effect in few-layer WTe_2, npj Comput. Mater. **5**, 119 (2019).